Journal of Geophysical Research: Solid Earth

RESEARCH ARTICLE
10.1029/2018JB016109

Modeling Trench Sediment-Controlled Flow in Subduction Channels: Implications for the Topographic Evolution of the Central Andean Fore Arc

N. J. Cosentino[1,2,3], J. P. Morgan[4], and T. E. Jordan[1]

[1]Department of Earth and Atmospheric Sciences, Cornell University, Ithaca, NY, USA, [2]Facultad de Ciencias Exactas, Físicas y Naturales, Universidad Nacional de Córdoba, Córdoba, Argentina, [3]Consejo Nacional de Investigaciones Científicas y Tecnológicas (CONICET), Centro de Investigaciones en Ciencias de la Tierra (CICTERRA), Córdoba, Argentina, [4]Department of Earth Sciences, Royal Holloway, University of London, Egham, UK

Abstract The high elevation of the onshore fore-arc platform in northern Chile cannot be accounted for by previously proposed tectonic mechanisms such as coastal underplating and coseismic deformation, whose topographic effects are restricted to the coastal zone. Subduction channels have been recognized both in modern and fossil noncollisional convergent margins, yet their role on fore-arc surface elevation has not been sufficiently explored. Long-term viscoelastic flow in a strengthened, finite-thickness subduction channel promotes coupled offshore fore-arc subsidence and onshore fore-arc platform uplift. We propose that the onset of protracted hyperaridity in the coastal zone of northern Chile starved the trench of sediments, inducing a rise in shear stress at the top of the subduction channel sufficient to trigger hundreds of meters of uplift of the onshore fore-arc basin surface, most of which took place by the middle Miocene. This is consistent with latitudinal correlations between coastal precipitation, trench sediment thickness and onshore fore-arc topography along the Chilean margin, and with available paleoclimatic and paleotopographic evidence in northern Chile.

Key Points:
- Trench fill sediments have been proposed to influence plate interface rheology and fore-arc elevation
- Strengthening the subduction channel promotes coupled long-wavelength onshore uplift and offshore subsidence in the fore arc
- Hyperaridity-induced sediment starvation in the trench may explain the highly elevated onshore fore-arc basin surface in northern Chile

Supporting Information:
- Supporting Information S1

Correspondence to:
N. J. Cosentino,
nicolas.cosentino@conicet.gov.ar

Citation:
Cosentino, N. J., Morgan, J. P., & Jordan, T. E. (2018). Modeling trench sediment-controlled flow in subduction channels: Implications for the topographic evolution of the central Andean fore arc. *Journal of Geophysical Research: Solid Earth*, *123*. https://doi.org/10.1029/2018JB016109

Received 16 MAY 2018
Accepted 21 SEP 2018
Accepted article online 26 SEP 2018

1. Introduction

At noncollisional subduction margins, the plate interface has been described as a finite thickness, variably consolidated sedimentary layer called a subduction channel (SC; e.g., Shreve & Cloos, 1986; Vannucchi et al., 2012). The main evidence supporting the existence of SCs in modern subduction margins is the seismic identification of a relatively low *P* wave velocity zone, less than 2 km in thickness, bounded by strong reflectors and that can be traced down to seismogenic depths in many margins (e.g., Bangs et al., 2015; Collot et al., 2011; Janiszewski & Abers, 2015; Ranero et al., 2008), including northern Chile (von Huene & Ranero, 2003).

The SC is thought to play a dynamic role in accommodating long-term mass flow between plates and in the downdip direction (e.g., Clift & Hartley, 2007), acting as a conveyor belt of sediments to depths greater than the updip end of the seismogenic zone. SCs deeper than the seismogenic zone have not been seismically imaged. Nonetheless, several lines of evidence support the idea that indeed SCs reach greater depths. First, arc lavas have geochemical and isotopic signatures suggestive of subducted sediments reaching the source region for arc magmas (e.g., Karig & Kay, 1981; Plank & Langmuir, 1998). Second, many models that try to explain the origin of enriched mantle domains require the injection of subducted sediments past the arc source in order to be consistent with chemical and isotopic composition constraints (e.g., Plank & Langmuir, 1998; Zindler & Hart, 1986). Finally, rapid exhumation of high *P*/*T* metamorphic rocks by return flow requires SCs that reach at least a depth of 100 km (e.g., England & Holland, 1979; Friederich et al., 2014).

A series of observations along the Andean margin suggest that SC material properties are important in determining the topographic profile between the trench and either the volcanic arc (Lamb & Davis, 2003) or, more restrictively, the eastern onshore fore-arc platform (Cosentino, Aron, et al., 2018). In agreement with this, previous modeling efforts suggest that the SC material properties control upper plate deformation to varying degrees (e.g., Sobolev & Babeyko, 2005; De Franco et al., 2006; Gerbault et al., 2009; van Dinther et al., 2012). This paper presents a new numerical model of SC flow and its fore-arc topographic signal. We show that SC strengthening (i.e., a rise in the average viscosity of the SC) produces coupled long-wavelength

offshore fore-arc subsidence and onshore fore-arc platform uplift. In particular, small variations in SC viscosity have a significant impact on the topographic signal of the fore arc. The time scale of the topographic responses is appropriate to explain certain paleotopographic constraints in northern Chile.

The Neogene phase of Nazca-South American plate convergence produced topography of the westernmost 1,000 km of South America that displays first-order similarities and second-order differences along more than 3,000 km of trench-parallel distance (Isacks, 1988). Numerous analyses have examined the mechanical causes of the full-orogen topographic patterns (e.g., Capitanio et al., 2011; Faccenna et al., 2017; Isacks, 1988; Lamb & Davis, 2003; Sobolev & Babeyko, 2005). Yet there is second-order variability of the total fore-arc relief and the existence of continental fore-arc basins that has not been adequately explained, and which is the focus of this study.

Cosentino, Aron, et al. (2018) note that along the Andean margin (19–40°S), onshore fore-arc elevations and trench depth are inversely correlated to trench sediment thickness and coastal precipitation (Figure 1). This suggests that subducted sediments, and indirectly climate, play a role in controlling plate-interface rheology, a link previously proposed by Lamb and Davis (2003). According to this hypothesis, at locations or time periods of wetter continental climate (Figure 2a), sediment transport to the trench is enhanced and the trench is relatively sediment-full. The SC is thus well fed with wet sediments that raise pore fluid pressure, counteracting normal stress, and reducing the frictional strength of SC materials. This lubricating effect results in weakening of the plate interface. If we assume the rheology of the SC to be viscoelastic (see section 2), then it is viscous strength that is reduced by enhanced sediment delivery to the SC. This viscous weakening results in a reduction of average SC viscosity, which becomes considerably lower than average fore-arc viscosity. Conversely, during periods of greater continental aridity (Figure 2b), sediment transport to the trench is reduced and the trench remains relatively starved. The SC is thus relatively devoid of wet sediments, so that the viscosity contrast between the SC and fore arc is smaller. This proposed connection between trench sediment and the mechanical properties of the plate interface hundreds of kilometers from the trench implies sediment transport from the trench along the plate interface to depths exceeding 100 km, as in the SC hypothesis itself.

In northern Chile between 19 and 21.5°S the fore arc is of typical width (~250–300 km) but of unusual total relief, from a trench axis ~6,700–7,600 m below sea level to the volcanic arc at maximum elevations $>$5,000 m above sea level (m asl; Figure 3). The western half of the profile is offshore and convex-up in form. Except for an abrupt coastal escarpment, from sea level to 500–1,200 m asl, the onshore fore arc essentially constitutes an 80-km-wide western platform at ~1,000 m asl and an eastern monocline that rises to the active volcanic arc. The physiography of the onshore platform includes a western relict mountain range, the Coastal Cordillera (CC), and an eastern fore-arc basin surface, the Central Depression (CD). The monocline includes the easternmost CD and the Western Andean Slope and accommodates fore-arc deformation due to uplift of the Altiplano Plateau to the east (Figure 3; Isacks, 1988).

Mortimer and Sarič (1975) recognized the onshore platform to be a low-relief erosional surface, the Tarapacá pediplain, whose eastern region is partially buried by fore-arc sediments. Stratigraphic relations (Mortimer & Sarič, 1975) and thermochronological data (Juez-Larré et al., 2010) concur that the low-relief surface formed during the Eocene and Oligocene. A low-relief erosional surface would not form perched 1,000 m above the nearby Pacific coastline but must instead have been uplifted after it formed close to sea level. Four hypotheses have been put forward to explain long-term surface uplift of the onshore platform: (a) plate convergence-driven interseismic compression in the upper plate (e.g., González et al., 2003), (b) coseismic deformation due to earthquakes originating at the plate interface below the continental Moho (Melnick, 2016), (c) underplating of subduction erosion-derived interplate sediments (e.g., Clift & Hartley, 2007), and (d) increased shear stresses along the plate interface linked to a paucity of sediments reaching the trench (Lamb & Davis, 2003). The first three mechanisms arguably have short-wavelength topographic effects that act to produce positive relief of the CC relative to both the CD and continental shelf (e.g., Clift & Hartley, 2007; González et al., 2003; Melnick, 2016). Instead, we hypothesize that the fourth mechanism is the main contributor to long-term surface uplift of the CD, west of the downdip monocline hinge.

Contrary to our hypothesis, previous numerical studies suggested that shear coupling at the plate interface has a secondary influence on Central Andean tectonic uplift (Sobolev & Babeyko, 2005). However, the objective of their study was to understand the factors that control tectonic shortening, rather than elevation.

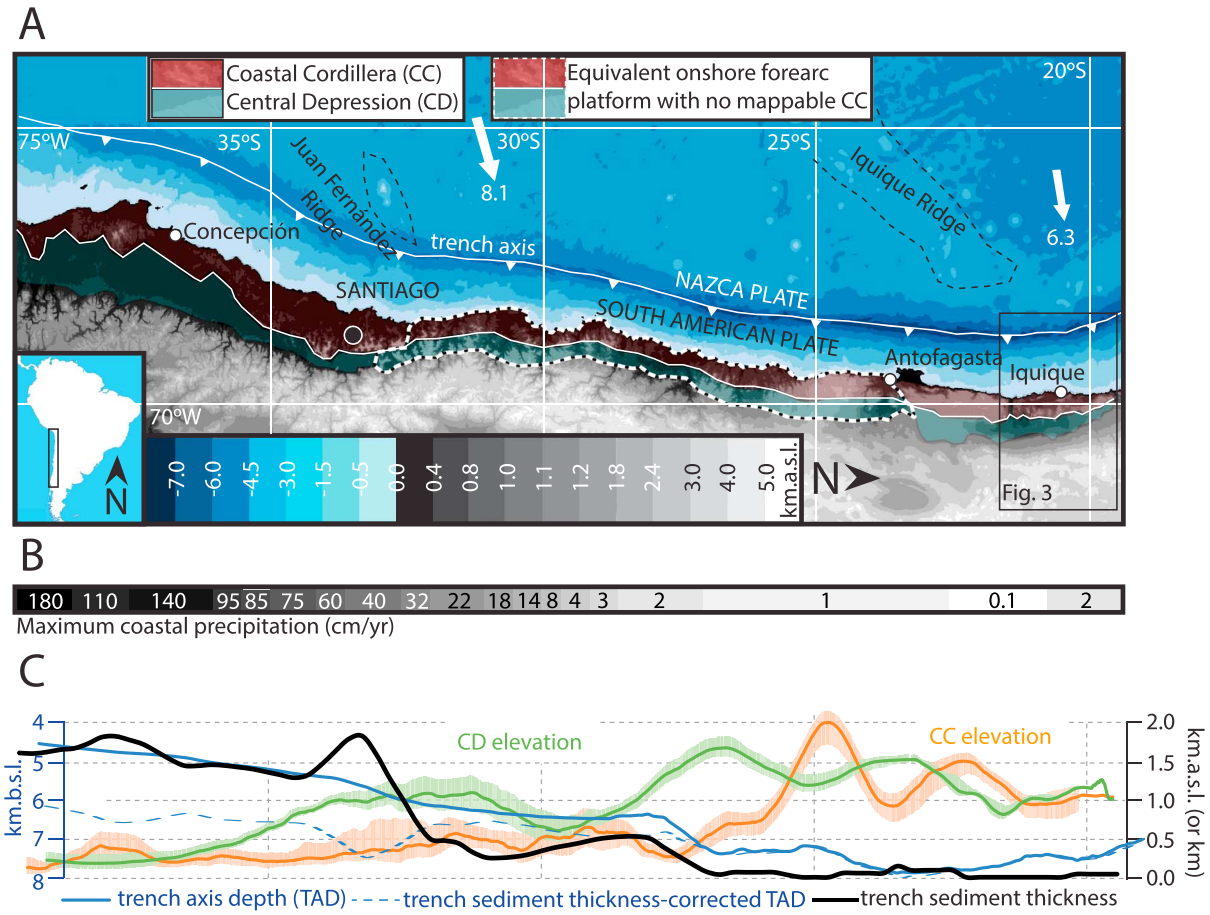

Figure 1. (a) Thirty-arc-second-resolution topography and bathymetry of the fore arc of the Andean subduction margin between 19 and 40°S (the GEBCO_2014 Grid, version 20141103, http://www.gebco.net). The Coastal Cordillera (CC) is mapped as the broad topographic ridge located between the coast and the position inland marked by a break in regional slope across the east-facing landscape. To the east, the Central Depression (CD) is mapped as a basin landscape with regional slope $< 1.5°$. There is a latitudinal band (24–33°S, inside white dashed line) where these mapping criteria fail to define the limit between the CC and CD. In this region, the CC-CD boundary is set so that these units have equal widths, a condition generally met north of this latitudinal band. The white arrows are convergence directions and rates (in cm/yr) of the Nazca plate with respect to the South American plate, based on DeMets et al. (1994). (b) Maximum coastal rainfall (Dirección Meteorológica de Chile, http://164.77.222.61/climatologia/). C(c) Longitudinal cross sections of topography and trench characteristics. Median elevations of the CC and CD (right scale) are extracted from latitudinal swath profiles performed across straight segments every 0.01° latitude, based on the method described by Hergarten et al. (2014) and with trench-perpendicular widths such that they cover the entirety of the mapped CC and CD units. In each of these units' cases, the digital elevation model outside the mapped area was set to not a number in order to better isolate their elevations. The color envelopes correspond to the 25th–75th percentile elevations. Thickness of sediment at the trench axis (thick black line, right scale), not including sediment rafted to the trench on the oceanic plate, is based on a compilation of seismic reflection profiles across the Nazca-South America trench (Schweller et al., 1981). The thick blue line corresponds to the maximum trench axis depth below sea level (left scale), and the dashed blue line to the TAS depth corrected for the thickness of the sedimentary package, so as to show the depth to the oceanic-continental plate basement contact (left scale). In all cases simple 1° moving window averages are shown. Modified from Cosentino, Aron, et al. (2018).

Besides, they considered shortening at the scale of the entire Central Andean transect, rather than examining the fore arc. In order to test our hypothesis, we concentrate on fore-arc elevation.

Here we experiment numerically on the effects of flow within a simplified SC in concert with the idea of climate change-driven million-year-scale variability in continental sediment input to the trench. We characterize the response of fore-arc surface elevation and test our results against modern fore-arc topography. We also explore the fit between the model results and available late Cenozoic surface paleoelevation constraints for northern Chile. Whereas climate-related sediment supply to the trench is what motivates this study, other phenomena such as seamount subduction could cause SC properties to vary laterally or through time at subduction margins. Hence, the numerical experiments presented here may have broad applicability.

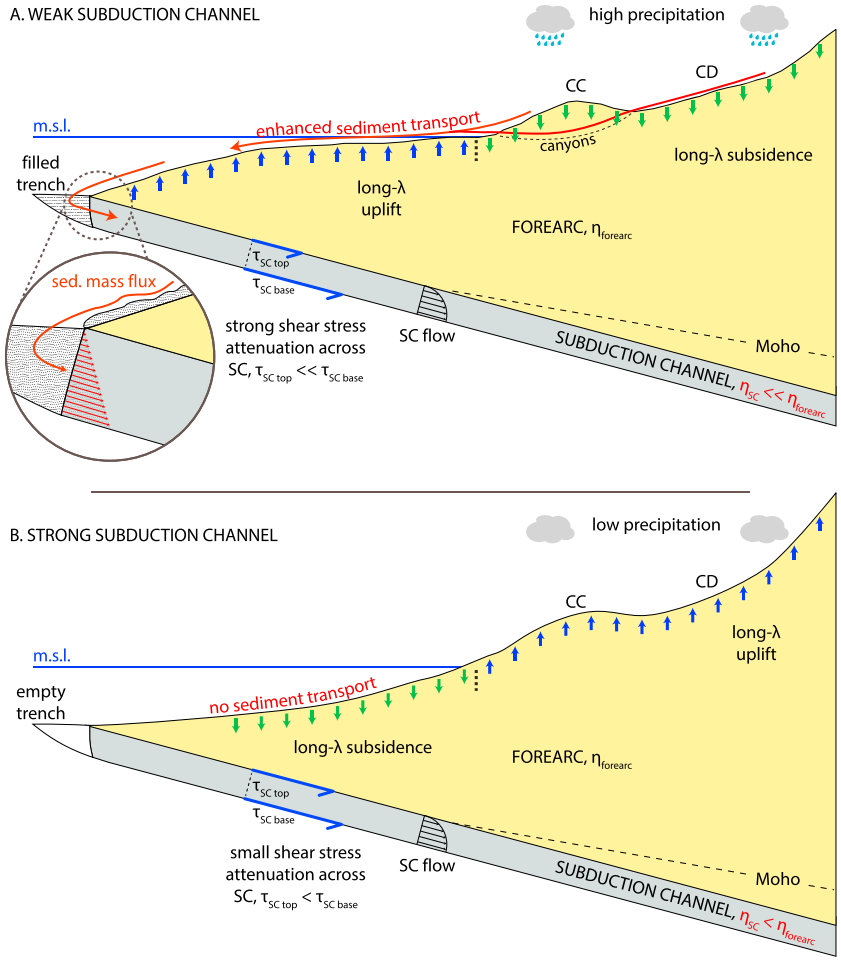

Figure 2. Schematic representation of the role of subducted sediments, and indirectly climate, on plate interface rheology and fore-arc elevation in the Nazca-South America plate margin. After a prolonged period of steady state upper plate elevations induced by constant subduction channel (SC) and upper plate parameters, a perturbation in SC strength (i.e., average viscosity) occurs, triggering changes in fore-arc elevation (see text for discussion). (a) During phases of wetter continental climate, enhanced sediment transport to the trench implies enhanced delivery of wet sediments to the SC, raising pore fluid pressure, reducing normal stress, and reducing the frictional strength of SC materials. Average SC viscosity becomes considerably lower than average fore-arc viscosity. These conditions trigger long-wavelength offshore fore-arc uplift and onshore fore-arc subsidence. (b) Conversely, during periods of greater continental aridity, sediment transport to the trench is reduced and the trench remains relatively starved. The SC is thus relatively devoid of wet sediments, so that the viscosity contrast between the SC and fore arc is smaller. These conditions favor long-wavelength offshore fore-arc subsidence and onshore fore-arc uplift. CC: Coastal Cordillera, CD: Central Depression, msl.: mean sea level. Modified from Cosentino, Aron, et al. (2018).

2. Methods

We model deformation in the SC and overriding plate as two-dimensional incompressible, Newtonian, isotropic, Stokes viscoelastic creeping flow under the influence of gravity in a Lagrangian finite element grid. SC flow in the trench-parallel direction is assumed to be small compared to flow along a plane normal to the trench axis. In this case, a 2-D treatment can capture the predominant forces acting on the channel (i.e., the shear forces applied by the subducting plate and gravity-derived forces). Even if SC and upper plate materials may present short-scale (i.e., grain size) anisotropies in viscosity, we further assume, like many others, that there is no such anisotropy when averaged over longer scales. Since mantle and crustal motions can be considered as highly viscous creeping over geologic time scales, all inertial forces are negligible during creep. We thus use the Stokes approximation to fluid flow. Finally, rocks can typically recover part of their deformation once stress disappears, so we use a viscoelastic rather than a purely viscous rheology. For

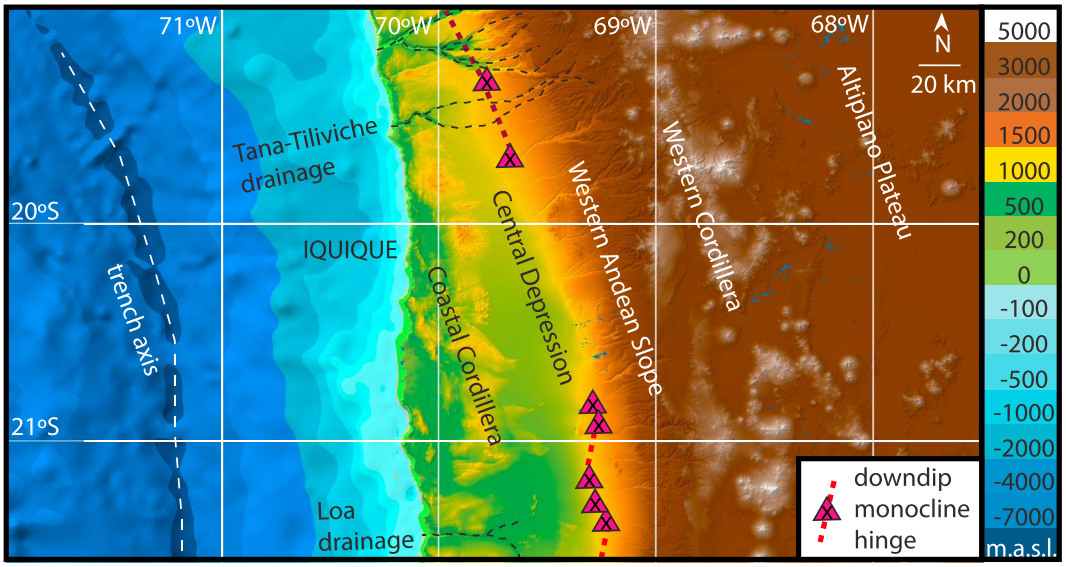

Figure 3. The Nazca-South America fore arc of the Central Andes of northern Chile. Bathymetry based on ETOPO1 and topography on SRTM-90. The western downdip monocline fold axes (black crosses in magenta triangles) and inferred hinge (red dashed line) defined according to Jordan et al. (2010). Exorheic drainages in the area are shown.

further simplicity in these initial models, we also assume a linear shear stress-shear rate relationship. A Newtonian rheology for the SC is consistent with the (micro) structural record of exhumed metamorphic rocks, which indicates that deformation is localized in low-strength shear zones dominated by dissolution precipitation creep or fluid-assisted granular flow (Gerya & Stöckhert, 2002).

Maximum average SC viscosities of 10^{18}–10^{20} Pa s are estimated based on assumptions of shear zone cumulative width, typical plate velocities, and stress provided by dislocation creep flow laws (Gerya et al., 2002; Stöckhert, 2002). At low temperatures, the main process by which SC sediments can increase their density significantly is by pore water loss and underplating to the upper plate (e.g., Shreve & Cloos, 1986). Consequently, the rest of the sediment still in the SC may be considered unaffected. We thus assume in our models that SC materials are incompressible, with a density ρ_{SC} = 2,200 kg m^{-3} (Figure 4 and Table 1).

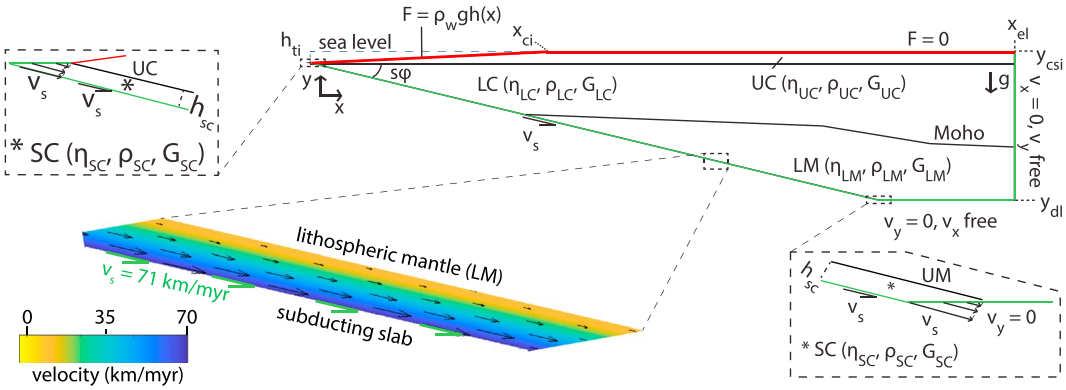

Figure 4. The geometry of the modeled domain is defined by the subduction angle ($s\varphi$), domain depth limit (y_{dl}), domain eastern limit (x_{el}), initial coastal position (x_{ci}), initial continental surface topography (y_{csi}), initial trench depth (h_{ti}), subduction channel (SC) thickness (h_{sc}), and upper crust (UC)-lower crust (LC) and Moho discontinuities (Table 1). Physical parameters are density (ρ), viscosity (η) and shear modulus (G; Table 1). Applied boundary conditions are either fixed velocity (green line) or applied forces (red line; Table 1). In the case of boundaries with fixed velocities, these impositions may be applied either to the horizontal component (right or arcward boundary), the vertical component (bottom boundary), or both components of velocity (SC bottom boundary, where the relative subduction velocity v_s is prescribed). Also shown is the velocity field within the SC after 6 myr of simulation time for a particular choice of parameters: (a) 500-m-thick SC with average viscosity of 7 × 10^{18} Pa s and v_s = 71 km/myr.

Table 1
Geometrical and Material Model Parameters

		Parameter	Value	Comments	Reference
Geometrical parameters	Fixed	Subduction angle ($s\varphi$, °)	23	Constant along the downdip direction	David et al. (2002)
		Subduction velocity (v_s, mm yr^{-1})	71	Orthogonal component of convergence rate	David et al. (2002)
		Initial trench depth (h_{ti}, km)	−7.45	20–21°S SRTM-90 average	
		Initial coastline (x_{ci}, km)	115	From trench	
		Eastern domain limit (x_{el}, km)	400	From trench	
		Initial inland topography (y_{csi}, m)	0	Everywhere	
		Depth domain limit (y_{dl}, km)	100		
		MOHO			Tassara et al. (2006); Cosentino, Morgan, et al. (2018)
		Upper crust-lower crust discontinuity			Tassara et al. (2006); Cosentino, Morgan, et al. (2018)
	Variable	Subduction channel thickness (h_{sc}, m)	350–1,100	Constant along the downdip direction	
Material parameters		Subduction channel viscosity (η_{SC}, ×10^{18} Pa s)	3–20	Homogeneous in space	
	Fixed	Sea water density (ρ_w, kg m^{-3})	1,020		
		Subduction channel density (ρ_{SC}, kg m^{-3})	2,200	Homogeneous in space and constant in time	Shreve and Cloos (1986)
		Upper crust density (ρ_{UC}, kg m^{-3})	2,700		Tassara et al. (2006)
		Lower crust density (ρ_{LC}, kg m^{-3})	3,100		Tassara et al. (2006)
		Lithospheric mantle density (ρ_{LM}, kg m^{-3})	3,240		Tassara et al. (2006)
		Subduction channel shear modulus (G_{SC}, ×10^9 Pa)	10		van Dinther et al. (2013)
		Upper crust shear modulus (G_{UC}, ×10^9 Pa)	25		van Dinther et al. (2013)
		Lower crust shear modulus (G_{LC}, ×10^9 Pa)	25		van Dinther et al. (2013)
		Lithospheric mantle shear modulus (G_{LM}, ×10^9 Pa)	67		van Dinther et al. (2013)
		Upper crust viscosity (η_{UC}, ×10^{21} Pa s)	82		Roy and Royden (2000)
		Lower crust viscosity (η_{LC}, ×10^{21} Pa s)	26		Roy and Royden (2000)
		Lithospheric mantle viscosity (η_{LM}, ×10^{21} Pa s)	1.7		Roy and Royden (2000)
Fixed		Time step (yr)	10,000		

The model geometry is a several hundred-meter-thick SC at the interface between the upper plate and subducting slab (Figure 4 and Table 1). This geometry is inferred from imaging of SCs as ~100- to 1,000-m-thick low-velocity layers (e.g., Sage et al., 2006). The lower model domain boundary is y_{dl} = 100 km, while the eastern model domain boundary is x_{el} = 400 km (Figure 4 and Table 1). The angle of subduction is fixed at $s\varphi$ = 23° (Figure 4 and Table 1). The Moho and upper crust-lower crust geometries are prescribed according to the Andean density model of Tassara et al. (2006; Figure 4 and Table 1; see also the supporting information), defining three upper plate domains: upper crust, lower crust, and lithospheric mantle. Compared to the SC, the upper plate is assumed to be comparatively rigid, at least 2 orders of magnitude more viscous (Table 1). Upper plate materials are also assumed to be incompressible.

Triangle C (Shewchuk, 1996) is used to generate ~10^5-element unstructured two-dimensional Delaunay triangular meshes after each time step for two subdomains: the SC and the upper plate (Figure 4). An ~250-m horizontal resolution is achieved along the free surfaces. We follow deformation of the atmosphere-land and seafloor free surfaces using 10-kyr time steps, wherein deformation results from shear stresses imposed on the SC top by the subducting slab, by flow in the SC, by buoyancy forces originating from differences in density between SC and fore-arc materials, and by the weight of the water column in the case of the seafloor surface. The initial configuration of the free surfaces is arbitrary for the sake of studying the long-term system response because the experiments reach a quasi- steady state elevation profile that is independent of the initial configuration (Figure 4 and Table 1). The only selection of initial configuration of the free surfaces that is intended to correspond to an expected geological constraint is that there is a point at which the top free surface passes from water to air.

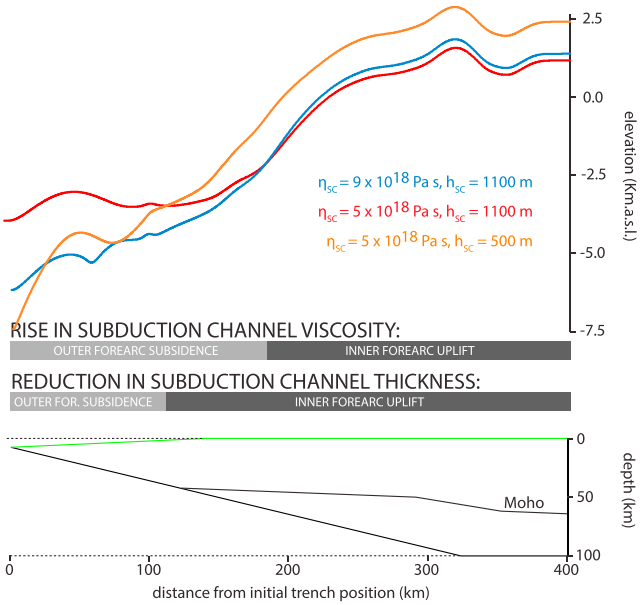

Figure 5. Modeled fore-arc elevations for at the conclusion of three selected 12-myr-long simulations. Both a rise in subduction channel (SC) average viscosity η_{SC} (compare red to blue lines) and a reduction in SC thickness h_{SC} (compare red to orange lines) promote outer fore-arc subsidence and inner fore-arc uplift. The horizontal bars indicate the spatial extent of net fore-arc uplift and subsidence when comparing final model elevation profiles for two simulations with equal h_{SC} and differing η_{SC} ("rise in subduction channel viscosity"), and vice versa ("reduction in subduction channel thickness"). The bottom drawing represents the initial model domain geometry, with the free surface boundary in green (flat inner fore-arc surface lying at 0 m above sea level and outer fore-arc surface linearly descending to the initial trench depth; see Figure 4 and Table 1 for exact values of the geometry parameters).

As with any boundary value problem for partial differential equations, for a well-constrained solution, additional boundary conditions need to be imposed onto the domain. Natural (i.e., force) boundary conditions are applied at the continental top free surface, along which a null force is prescribed, and at the marine surface, where a force corresponding to the overlying water column's weight is prescribed. Essential (i.e., fixed velocity) boundary conditions are applied to the rest of the boundaries of the domain. The slab is represented by a fixed velocity boundary condition corresponding to the relative convergence rate, v_s = 7.1 cm yr^{-1}, applied at the bottom of the SC (Figure 4 and Table 1). A null vertical and horizontal velocity component is prescribed to the lower and eastern (i.e., right) model boundaries, respectively (Figure 4). Also, a shear-like velocity profile is applied at the SC inlet (see Figure 4, upper left box), representing mass flow into the SC. Mass conservation within the SC is achieved by applying the same velocity profile at the SC downdip end (see Figure 4, lower right box).

We use MILAMIN, a MATLAB-based finite element method mechanical solver (Dabrowski et al., 2008), modified to include the viscoelasticity terms. The incompressibility constraint is achieved through an iterative penalty method. A relatively small penalty factor κ is used, guaranteeing a good condition number, and incompressibility of flow is achieved by Powell/Hestenes/Uzawa-type iterations (Dabrowski et al., 2008), which is also known as an Augmented Lagrangian formulation. See the supporting information for details on the formulation of viscoelastic fluid flow and general code structure. The full code is available as open source (Cosentino, Morgan, et al., 2018).

We performed 18 runs with SC viscosity (η_{SC}) varying between 3 and 20 × 10^{18} Pa s and SC thickness (h_{SC}) varying between 350 and 1,100 m, both of which are constant throughout each run. We also performed 8 runs with starting η_{SC} = 7 × 10^{18} Pa s and h_{SC} = 500 m, to which after 4 myr were applied 1-myr-long pulses of higher or lower η_{SC} that migrate downdip in the SC with the velocity of relative subduction (Table 1). We do this in order to emulate phases of varying sediment delivery to the trench. In all cases, simulations were run for a total of 12 myr, an amount of time that was found to be sufficient to reach steady state conditions and subsequently characterize the processes of interest.

3. Results

The main effect of SC strengthening (i.e., a rise in average SC viscosity, η_{SC}) on topography is a rise in total relief between the trench and the eastern model boundary. This rise is due both to a deeper trench and to a higher elevation eastern boundary (Figure 5). These relationships are linear across the range of modeled viscosities (Figures 6a and 6b). In particular, small variations in SC viscosity have a considerable impact on fore-arc topography. Topographic relief from the trench to the eastern model boundary also grows with decreasing SC thickness (h_{SC}; Figures 5 and 6a and 6b). The integrated shear force along the SC roof has a positive linear correlation with η_{SC} and an inverse correlation with h_{SC} (Figure 6c).

All 18 simulations with constant-in-time SC viscosity (η_{SC}) and thickness have an initial coastline (elevation of 0 m asl) at (x_{ci}) 115 km from the trench (Figure 4 and Table 1), which evolves toward an approximately steady state position. Consequently, each simulation locates its own shoreline position as an integrated result of the shear stresses, flow within the SC, buoyancy forces, and the weight/pressure of the water column. Measured from each simulation's end-of-run coastline position, the two simulations that best fit the CD west of the monocline have SCs with a thickness of 1,100 m and viscosities of 9–10 × 10^{18} Pa s (Figures 6d and 7). None of the simulations achieves the high-gradient, short-wavelength elevation change of the coastal escarpment, while a third of the runs show an eastward reduction in elevation east of 85–100 km from the coast (Figure 7). Also, experiments with placement of the eastern domain boundary farther from the initial

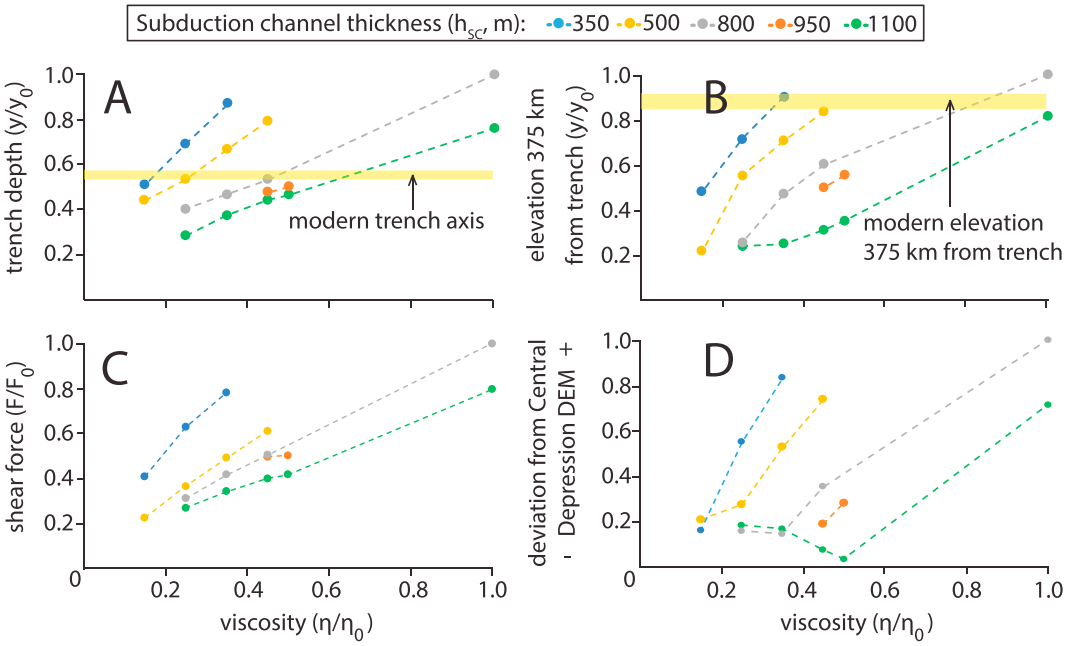

Figure 6. (a) Depth of trench, (b) elevation 375 km from the trench, and (c) integrated subduction channel roof shear force per parallel-to-trench unit length, versus subduction channel (SC) average viscosity. (d) Comparison of Central Depression topography with modeled elevations between 30- and 95-km inland from each end-of-run coastline position, where the sum of differences in topography between each model's final output and DEM is calculated and normalized with respect to the model with the highest sum. Elevations and shear force are normalized to those of the model with an 800-m-thick SC with an average viscosity $\eta_0 = 2 \times 10^{19}$ Pa s. Values are calculated after 12 myr of simulation run time.

trench than the 400 km distance ultimately selected to use for all simulations caused a reduction in elevations throughout the fore arc (see the supporting information), probably due to stress dispersion.

The initial high rates of uplift result from the fact that the initial onshore free surface configuration (flat 0 m asl elevation) is very different to each model run's steady state configuration. Rates of surface elevation change across the onshore fore-arc platform are close to zero after ~4 myr, effectively reaching a quasi-steady state

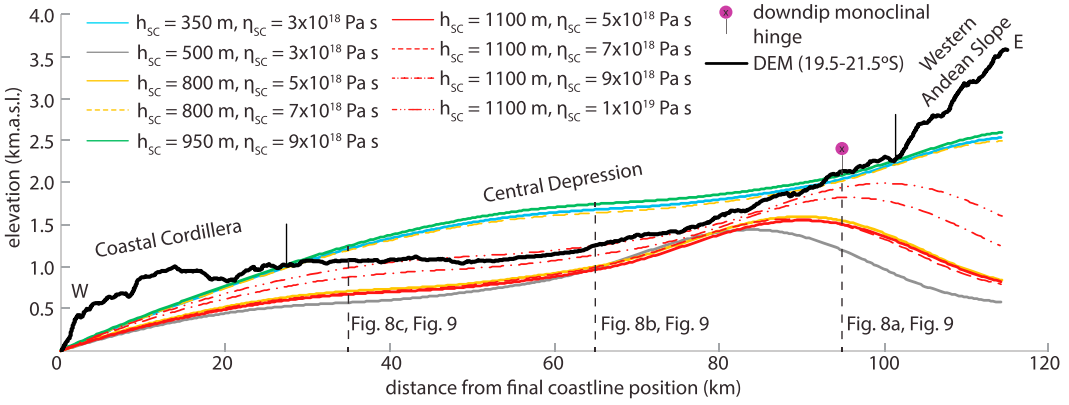

Figure 7. Final topography of 12-myr-long simulations (colored lines) compared to modern elevation (DEM curve). The modeled elevation profiles span subduction channel (SC) thicknesses (h_{SC}) of 350–1,100 m and constant, homogeneous SC viscosities (η_{SC}) of 3–10 × 10^{18} Pa s. The nine simulations that best fit the elevation of the Central Depression are shown (see Figure 6d). Horizontal distance is measured with respect to the modern coastline position (DEM curve) or to each end-of-run coastline position (model curves). The DEM curve consists of the average of elevations along trench-perpendicular profiles at 19.53°S, 20.00°S, 20.50°S, 21.00°S, and 21.44°S (SRTM-90). The downdip monoclinal hinge is defined as the average hinge position between 20.75°S and 21.75°S (Jordan et al., 2010).

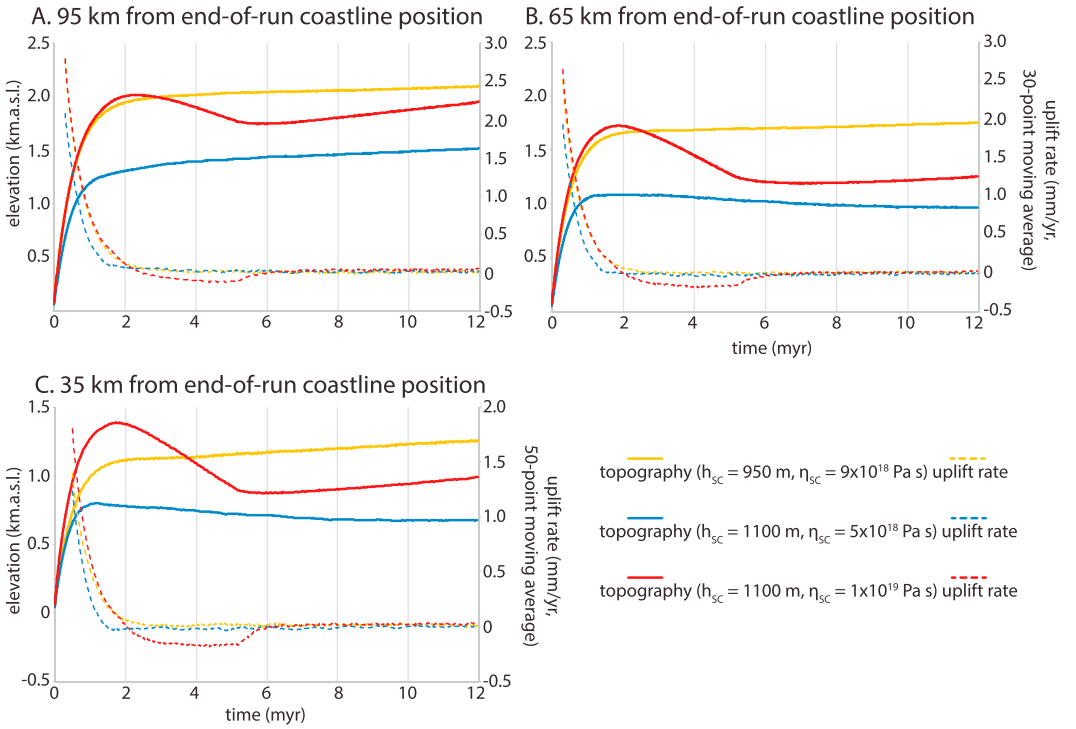

Figure 8. Evolution of surface elevation and uplift rate at (a) 95 km, (b) 65 km, and (c) 35 km from the final coastline position (see Figure 6), for three selected simulations. The horizontal axis is model time after initiation with an arbitrary elevation profile.

(Figure 8). The effect on surface elevation of applying 1-myr-long pulses of SC material with different viscosity is transient (Figure 9). For a 500-m-thick SC with steady state average viscosity of 7×10^{18} Pa s, to which are applied viscosity pulses $\Delta\eta$ of $1–3 \times 10^{18}$ Pa s, the maximum continental surface elevation change is ~400 m). This topographic change is similar throughout the onshore fore-arc platform and is achieved first at locations close to the coastline, lagging by 1.3–2.2 myr after the end of the event (Figure 9). Between 85 and 90% of the transient effect of SC pulses on surface elevation is lost within 2.6–4 myr after the end of the pulse, with the time lapse varying with position (Figure 9).

4. Discussion

West of the Central Andes, mass removal processes such as tectonic erosion of the upper plate close to the trench (e.g., von Huene & Lallemand, 1990; von Huene & Ranero, 2003) coupled with mass accretion processes such as underplating beneath the coastal region (e.g., Clift & Hartley, 2007) have been put forward as mechanisms to explain coupled, localized long-term net surface subsidence of the offshore fore arc and uplift of the westernmost onshore fore-arc platform. This study proposes an alternative geodynamic mechanism that explains these coupled phenomena at a scale that pertains to the entire trench-perpendicular extent of the offshore fore arc and onshore fore-arc platform.

An important mechanical effect of the SC is to modulate the shear stress applied by the subducting slab to the upper plate. The lower the viscosity of the SC or the greater its thickness, the greater the fraction of differential plate motion that is consumed in straining SC materials, and the smaller the fraction of shear stress transmitted across the SC from the subducting slab to the overriding plate (Figure 6c). The calculated shear force integrated along the SC top after 12 myr is in the range of $2–9 \times 10^{12}$ N per unit length in the direction parallel to the trench. This range is in line with previous estimates between 5 and 45°S latitude, based on an analytical approach (Lamb & Davis, 2003) that assumed the length of the SC top (249 km) to be approximately that of our modeled plate interface (256 km).

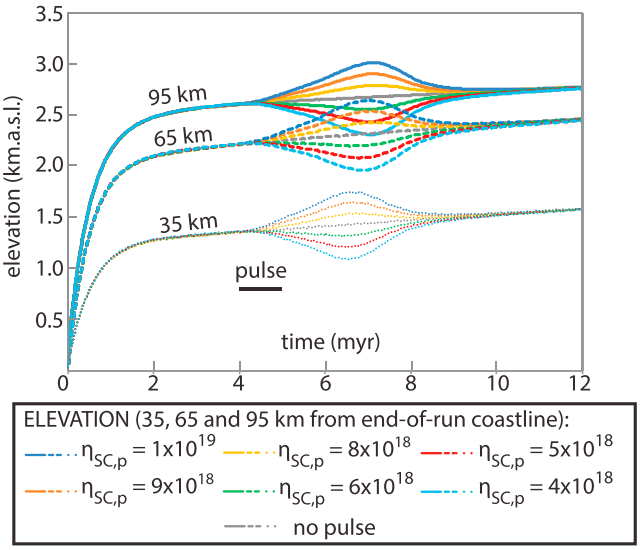

Figure 9. Evolution of surface elevation at 35, 65, and 95 km from the final coastline position (see Figure 6), for a 500-m-thick subduction channel with a viscosity of 7×10^{18} Pa s. Also shown are simulations that include 1-myr-long pulses from 4 to 5 myr after the start of the run of differing viscosity that migrate downdip in the subduction channel with the velocity of relative subduction.

When measured from the end-of-run coastline, simulations that best fit northern Chile CD elevations (Figure 6d) greatly underestimate elevation east of the CD (i.e., to the right of ~90 km from the coast; Figure 7). This result is consistent with the design of the modeled system to fit the processes of the fore arc, not an entire orogenic belt. In the Central Andes, the Western Andean Slope and easternmost CD is a monocline that uplifted in response to uplift of the Altiplano Plateau (Isacks, 1988), and the monocline lower hinge is located ~95 km from the coast (Jordan et al., 2010; Figure 7). We conclude that, east of a position ~85–95 km from the coast, surface elevation primarily responds to the processes that uplift the Altiplano Plateau instead of to the local forces transmitted across the SC.

It is important to mention that the position of the eastern domain boundary has an influence on elevations across the fore arc: the further to the east the model boundary, the lower the elevations. Nonetheless, our choice of 400 km from the initial trench position as the eastern model boundary is consistent with independent empirical information. Ward et al. (2013) showed a relatively abrupt change in subsurface shear velocities in the Central Andes at 22°S, from high values to the west to low values to the east, which should represent a natural barrier to stress dispersion. At depths of 15 km and shallower, the shear velocity boundary lies less than 300 km from the trench, whereas for depths of 30 and 50 km, it lies approximately 400 km from the trench.

von Huene et al. (2004) hypothesize that the weak material in a SC develops not only from trench sediment but also from abrasion of crust at the plate interface due to subducting slab roughness. They contend that this abrasive activity may explain why sediment-starved sections of the Chilean margin such as at 23.4°S (Figure 1) have SC thicknesses that are interpreted to be >1 km (von Huene & Ranero, 2003). Model simulations for SC thicknesses of 800–1,100 m fit best CD elevations in northern Chile and are in line with von Huene and Ranero's (2003) data (Figure 7). In addition to contributions to a SC from abrasion, space and time variations in detrital sediment influx from continental surface erosion may play a role in shaping topography and merit further investigation.

Two empirical approaches can be taken to testing the hypothesis that sediment starvation at the Perú-Chile trench induced fore-arc uplift in northern Chile: (1) investigation of whether temporal changes in sediment supply are matched by uplift or subsidence and (2) along-strike co-variations of sediment supply, which is dictated by climate or drainage basin size and topography (Cosentino, Aron, et al., 2018; Figure 1). Madella et al. (2016) combined both approaches: They show that throughout the Miocene to Quaternary the zone immediately north of our study area remained topographically low while the areas to the north and south increased in elevation and that its low relative elevation resulted in a positive feedback with supply of sediments from drainage basins to the trench.

If sustained high shear stresses across the SC result from hyperarid environmental conditions, then the time of onset of hyperarid climate should also be a time of broad-scale elevation change. The history of changes of absolute surface elevation has been constrained by a few studies of the CD in northern Chile. Cosentino et al. (2015) and Cosentino and Jordan (2017) used the bimodal distribution in elevation of Miocene to Holocene pedogenic calcium sulfate $^{87}Sr/^{86}Sr$ between 19.5 and 21.7°S to deduce that at least 45% of the elevation of the CD existed prior to the earliest Pliocene. Regarding paleoaltitudes during the middle Miocene, Evenstar et al. (2015) used the altitude control on the production rate of cosmogenic nuclides to conclude that more than 50% of the eastern CD elevation at 19.6°S existed prior to 13.4 Ma. Earlier paleoaltitude knowledge is sketchy, beyond the fundamental constraint that the Tarapacá pediplain formed above and close to sea level (Mortimer & Sarič, 1975). Based on a small set of observations of the modern elevation of the contact between the basement and the Oligo-Miocene fore-arc basin continental strata, a maximum net uplift of 840–1,000 m could have taken place in the CD at 19–19.6°S since >20 Ma (Table 2). Further south between 20.6 and 21.2°S, only 300 m of

Table 2
Contact Between Fore-Arc Basin Strata and Basement Underneath the Central Depression (CD) in Northern Chile (19–21.5°S)

Latitude (°S); distance inland (km)	Location in CD subareas	Basement-basin strata contact elevation (m asl)	Elevation of nearby fore-arc surface (m asl)	Age constraints on strata	Sources
19; 54 (Quebrada Camarones)	~Mean value of CD	1,000–1,150	2,140	>20 Ma (lower Oxaya Fm.)	
19.3; 33 (Tana well)	Central high-elevation region (200 m above mean)	840	1,270–1,280	>20 Ma (Azapa Fm.?)	ENAP well report; seismic 99-01 interpretation (Jordan); García and Fuentes (2012)
19.6; 30 (Dolores well)	Central high-elevation region (200 m above mean)	930–1,040	1,127	Azapa Fm. or lower El Diablo Fm.?	ENAP well report; depth range based on uncertainty about correct stratigraphic assignment of limestone, which could be either Jurassic (ENAP interpretation) or Miocene "lower El Diablo"
20.6; 65 (Pintados 1 and 2 wells)	~Mean value of CD	300–420	1,000	>20 Ma	Nester (2008); Blanco and Tomlinson (2013)
21.2; 70 (Soledad well)	Southern low-elevation region (200 m below mean)	310	910	>20 Ma	Nester (2008) and ENAP well report
21.5; 65 (Hilaricos well)	~Mean value of CD	25	955	>14 Ma	Nester (2008) and ENAP well report

uplift is permissible since >20 Ma, while at 21.5°S, this amount is further reduced to only 25 m since >14 Ma (Table 2).

Much of the documentation of the history of northern Chile's hyperaridity focuses on the CD and Andes during the Neogene (e.g., Evenstar et al., 2017; Hartley & Rice, 2005; Jordan et al., 2014; Sillitoe & McKee, 1996) and reveals that hyperarid conditions have been common since 23 Ma (Evenstar et al., 2017) and have predominated since ca. 12 ± 1 Ma (Jordan et al., 2014). Since then, three main short-lived wetter periods occurred, albeit still arid to semiarid, each lasting a million years or less, between 5.5–4.5 Ma, 4.0–3.6 Ma, and 2.6–2.2 Ma, as well as repeated intervals during the last 1 myr (Jordan et al., 2014). The recorded variability in Neogene CD and Andes climatic conditions may be translated to variability in sediment delivery to the trench (Madella et al., 2016). If so, then our model results for 1-myr-long pulses of less viscous material properties migrating down the SC make predictions about the deviations of onshore fore-arc platform elevations with respect to steady state, hyperarid continental conditions, both in terms of magnitude and timing across the onshore fore-arc platform (Figure 9). More specifically, our models predict that several-hundred-meter subsidence is associated to a 1-myr-long phase of less arid continental conditions. This topographic signal propagates across the onshore fore-arc platform from the coast toward the arc, with maximum elevations at the coastline lagging 1.3 to 2.2 myr after the end of the phase. This effect on fore-arc topography is transient, with surface elevation returning to almost steady state elevations 2.5 to 4 myr after the end of the phase. The spatial and temporal resolutions of existing paleoaltitude proxies in the Atacama are, nonetheless, insufficient to test our predicted changes in surface elevation due to pulsed SC flow as a consequence of variations in continental climate.

A significant fraction of the early and middle Miocene Andean sediment load was retained in the fore-arc basins (Evenstar et al., 2017; García et al., 2011; Jordan et al., 2010; Schlunegger et al., 2010). Consequently, we reason that it is the climate history of the CC that is most directly connected to sediment supply to the trench during the Neogene. In the CC, Dunai et al. (2005) and Schlunegger et al. (2010) interpreted the onset of hyperaridity at 20–25 Ma. However, earlier phases of aridification may also be possible, in relation, for example, to the Eocene global cooling trend (Lamb & Davis, 2003; Zachos et al., 2001).

In summary, for northern Chile, the timing of onset of CC hyperarity is similar to the timing of CD uplift, both demonstrated to have occurred during the late Oligocene to early Miocene. The general timing of the two phenomena is consistent with the hypothetical causality between uplift and sediment starvation in the trench caused by aridification. Yet neither the history of paleoelevations of the onshore fore-arc

platform nor the history of hyperaridity is as yet sufficiently resolved to be able to rigorously test this causality.

Potentially, these experiments on the impacts of SC properties are relevant to the subduction of oceanic plateaus and seamounts, which have also been demonstrated to impact fore-arc elevations (Geersen et al., 2015; Ranero & von Huene, 2000). Oceanic plateau subduction would be a prolonged phenomenon at a particular location along a continental margin, and it may impact the accumulation of sediment in the trench by deflecting away from the centerline of the plateau both continental drainages and within-trench currents. If so, the centerline of the subducting plateau may have a SC with less water-rich sediment than beyond the margins of the plateau, which would create a tendency for subsidence of the near-trench fore arc and uplift of the onshore fore arc. Nevertheless, this SC flow-generated topographic tendency may be overshadowed by other competing processes related to the plateau subduction, and thus, a careful analysis of examples is required. For the case of seamount subduction, there may be an analogy to the downdip migrating, 1-myr-long pulses of differing SC viscosity presented here. Seamount subduction beneath the northern Chile fore arc (Geersen et al., 2015) is well documented, but studies have not yet been conducted to examine whether there is coupled uplift of the onshore fore arc and subsidence of the near-trench fore arc that tracks seamount subduction. Further study of both situations is warranted.

Our model treatment examines one specific plate interface mechanism, SC viscoelastic flow. As such, the model results on fore-arc elevation presented here should be interpreted as characteristic of this mechanism in isolation. A number of other mechanisms that act at the plate interface have been anticipated to also impact fore-arc elevation. The most obvious ones are those that can explain the abrupt (i.e., short-wavelength) elevation gain at the coastal escarpment, an effect that is not reproduced by our models (Figure 7). Candidate local mechanisms include coseismic deformation during interplate earthquakes originating beneath the continental Moho (Melnick, 2016) and coastal underplating (e.g., Clift & Hartley, 2007). Another mechanism not incorporated in our models is tectonic erosion (e.g., Lallemand et al., 1994; von Huene & Ranero, 2003), which produces localized subsidence in the offshore fore arc. Coupling between the subducting slab and the upper plate will also depend on the magnitude of the slab pull force (Butler & Beaumont, 2017). A higher slab pull force is conducive to higher rates of onshore fore-arc uplift, thus acting in the same sense as a strengthening SC. The effect of the slab pull force on offshore fore-arc bathymetry is, however, less clear. The convergence rate is controlled in part, but not entirely, by the magnitude of the slab pull force. A rise in convergence rate has been demonstrated to raise plate interface brittle strength through a rheological feedback with temperature and strain rate (Dal Zilio et al., 2018). We thus expect reported changes in convergence rate in the Central Andes since the late Miocene (Somoza, 1998) to have affected fore-arc topography.

Another limitation of our model is related to the fact that the base of the SC, that is, the top of the subducting slab, is represented by a fixed boundary condition (Figure 4) and, as such, is not allowed to move vertically or tilt in response to modifications of the mass distribution within the model domain. We anticipate that our simplifying neglect of this potential feedback will tend to bias the models toward overestimations of the topographic relief across the fore arc, although the stronger slab should respond much more to changes in slab-pull and slab-bending forces than to the smaller shear-force component that is associated with the SC. For example, the relatively small postseismic uplift that follows a megathrust event provides a hint to the vertical motion of the incoming plate that can be linked to variations in shear stress along the SC.

Our model includes a series of simplifying assumptions of the many physical processes believed to take place in SCs (see section 2). Some of these assumptions might have an impact on the long-term topographic response of the fore arc discussed above. Three are of particular interest. First, our viscoelastic treatment of rheology implies that shear is partitioned uniformly across the SC. However, shear can be localized on multiple simultaneously active adjacent fault zones, which implies that rheology is more complex than purely viscoelastic (Fagereng & Sibson, 2010; Vannucchi et al., 2008). This more complex rheology within the SC might have important consequences on the transmission of shear stress across the SC and thus on the topographic response of the upper plate. Second, even under a purely viscoelastic SC rheology, a nonlinear SC viscosity may result in high strain rates localized within a region much thinner than the imposed thickness of the SC. This localization of strain rate might explain why our models are not able to capture the short-wavelength topographic signal characteristic of the coastal escarpment in northern Chile. Third, a two-phase,

compressible viscoelastic flow model would constitute a more accurate way of representing the physical processes acting in SCs, enabling density changes through pore water loss and underplating of SC materials to the upper plate. This, in turn, would result in dynamic variations of SC thickness in the downdip direction and thus variations in the topographic signal of the fore arc.

Along the Chilean margin, CD elevation correlates negatively with coastal precipitation and trench sediment thickness (Figure 1): The higher the CD, the lower the rainfall and the thinner the trench sediment. This geographic correspondence matches the numerical simulation results presented here. The match suggests that, despite model simplifications, coupled continental aridification, trench sediment starvation and strengthening of the SC, is a candidate mechanism to explain coupled long-term, long-wavelength offshore fore-arc subsidence and onshore fore-arc platform uplift.

5. Conclusions

Viscoelastic flow in a strengthening SC, in which average viscosity increases in response to a reduction in sediment delivery to the trench, is a numerically plausible geodynamic mechanism that explains coupled long-wavelength offshore fore-arc subsidence and onshore fore-arc platform uplift in subduction margins. Small variations in SC viscosity have a considerable impact on fore-arc topography. SCs act to modulate the shear force applied by the subducting slab to the upper plate: When a thick and weak SC is sustainable, it can significantly reduce the slab shear available to generate topographic relief.

This mechanism may be directly applicable to explain the latitudinal variability of fore-arc elevation along the Chilean margin, where latitudinally varying continental climate is probably responsible for sediment flow to the trench and SC rheology. Even if the paleoelevation history of northern Chile's onshore fore arc remains insufficiently resolved to test rigorously a causal link between climate and tectonics prior to the middle Miocene, our modeling results are consistent with a scenario where the onset of hyperaridity in the onshore fore-arc platform triggered a reduction in SC thickness and/or a rise in average SC viscosity. This resulted in hundreds of meters of uplift of the CD, which approached during the Miocene elevations close to its modern elevation.

Acknowledgments
Financial support was provided by the National Science Foundation award EAR-1049978 to T.E.J. and J.P.M. Lars Ruepke, Chao Shi, and Miguel A. Martínez contributed to the development of the numerical codes. We thank Louis Derry for computing time and Romain Vaucher for help with figure design. Finally, we thank editor Martha Savage as well as Jonas B. Ruh and an anonymous reviewer for their insightful comments, from which our manuscript has greatly benefited. Data supporting the conclusions of this contribution may be obtained from included tables and figures. Our code is fully available from Cosentino, Morgan, et al. (2018).

References

Bangs, N. L., McIntosh, K. D., Silver, E. A., Kluesner, J. W., & Ranero, C. R. (2015). Fluid accumulation along the Costa Rica subduction thrust and development of the seismogenic zone. *Journal of Geophysical Research: Solid Earth*, *120*, 67–86. https://doi.org/10.1002/2014jb011265

Blanco, N., & Tomlinson, A. (2013). Carta Guatacondo, Región de Tarapacá. Servicio Nacional de Geología y Minería, Carta Geológica de Chile, Serie Geológica Básica, p. 1. Mapa de escala 1:100,000, Santiago.

Butler, J. P., & Beaumont, C. (2017). Subduction zone decoupling/retreat modeling explains South Tibet (Xigaze) and other supra-subduction zone ophiolites and their UHP mineral phases. *Earth and Planetary Science Letters*, *463*, 101–117. https://doi.org/10.1016/j.epsl.2017.01.025

Capitanio, F. A., Faccenna, C., Zlotnik, S., & Stegman, D. R. (2011). Subduction dynamics and the origin of Andean orogeny and the Bolivian orocline. *Nature*, *480*(7375), 83–86. https://doi.org/10.1038/nature10596

Clift, P. D., & Hartley, A. J. (2007). Slow rates of subduction erosion and coastal underplating along the Andean margin of Chile and Peru. *Geology*, *35*(6), 503–506. https://doi.org/10.1130/G23584A.1

Collot, J. -Y., Ribodetti, A., Agudelo, W., & Sage, F. (2011). The South Ecuador subduction channel: Evidence for a dynamic mega-shear zone from 2D fine-scale seismic reflection imaging and implications for material transfer. *Journal of Geophysical Research*, *116*, B11102. https://doi.org/10.1029/2011jb008429

Cosentino, N. J., Aron, F., Crempien, J. G. F., & Jordan, T. E. (2018). Role of subducted sediments in plate interface dynamics as constrained by Andean forearc (paleo) topography. In R. V. Ingersoll, S. A. Graham, & T. F. Lawton (Eds.), *Tectonics, sedimentary basins, and provenance: A celebration of William R. Dickinson's Career* (chap. 3, Vol. 540, pp. 1–21). Boulder, CO: The Geological Society of America. https://doi.org/10.1130/2018.2540(03)

Cosentino, N. J., & Jordan, T. E. (2017). $^{87}Sr/^{86}Sr$ of calcium sulfate in ancient soils of hyperarid settings as a paleoaltitude proxy: Pliocene to Quaternary constraints for northern Chile (19.5-21.7°S). *Tectonics*, *36*, 137–162. https://doi.org/10.1002/2016TC004185

Cosentino, N. J., Jordan, T. E., Derry, L. A., & Morgan, J. P. (2015). $^{87}Sr/^{86}Sr$ in recent accumulations of calcium sulfate on landscapes of hyperarid settings: A bimodal altitudinal dependence for northern Chile (19.5°S–21.5°S). *Geochemistry, Geophysics, Geosystems*, *16*, 4311–4328. https://doi.org/10.1002/2015GC005954

Cosentino, N. J., Morgan, J. P., Rüpke, L. H., Andrés-Martínez, M., & Shi, C. (2018). Forearc topographic response to viscoelastic flow in subduction channels: A 2D finite element code for MATLAB. *Zenodo*. https://doi.org/10.5281/zenodo.1314752

Dabrowski, M., Krotkiewski, M., & Schmid, D. W. (2008). MILAMIN: MATLAB-based finite element method solver for large problems. *Geochemistry, Geophysics, Geosystems*, *9*, Q04030. https://doi.org/10.1029/2007GC001719

Dal Zilio, L., van Dinther, Y., Gerya, T. V., & Pranger, C. C. (2018). Seismic behaviour of mountain belts controlled by plate convergence rate. *Earth and Planetary Science Letters*, *482*, 81–92. https://doi.org/10.1016/j.epsl.2017.10.053

David, C., Comte, D., Martinod, J., Dorbath, L., Hérail, G., Dorbath, C., & et al. (2002), Intracontinental seismicity and Neogene deformation of the Andean forearc in the region of Arica, (18.5°S–19.5°S), paper presented at Fifth International Symposium on Andean Geodynamics, Dep. de Geofis., Univ. de Chile, Toulouse, France.

De Franco, R., Govers, R., & Wortel, R. (2006). Numerical comparison of different convergent plate contacts: Subduction channel and subduction fault. *Geophysical Journal International*, *171*(1), 435–450. https://doi.org/10.1111/j.1365-246X.2006.03498.x

DeMets, C., Gordon, R. G., Argus, D. F., & Stein, S. (1994). Effect of recent revisions to the geomagnetic reversal time scale on estimate of current plate motions. *Geophysical Research Letters*, *21*(20), 2191–2194. https://doi.org/10.1029/94GL02118

van Dinther, Y., Morra, G., Funiciello, F., Rossetti, F., & Faccenna, C. (2012). Exhumation and subduction erosion in orogenic wedges: Insights from numerical models. *Geochemistry, Geophysics, Geosystems*, *13*, Q06003. https://doi.org/10.1029/2011gc004011

Dunai, T. J., González López, G. A., & Juez-Larré, J. (2005). Oligocene-Miocene age of aridity in the Atacama Desert revealed by exposure dating of erosion-sensitive landforms. *Geology*, *33*(4), 321–324. https://doi.org/10.1130/g21184.1

England, P. C., & Holland, T. J. B. (1979). Archimedes and the Tauern eclogites: The role of buoyancy in the preservation of exotic eclogite blocks. *Earth and Planetary Science Letters*, *44*(2), 287–294. https://doi.org/10.1016/0012-821x(79)90177-8

Evenstar, L. A., Mather, A. E., Hartley, A. J., Stuart, F. M., Sparks, R. S. J., & Cooper, F. J. (2017). Geomorphology on geologic timescales: Evolution of the late Cenozoic Pacific paleosurface in Northern Chile and Southern Peru. *Earth-Science Reviews*, *171*, 1–27. https://doi.org/10.1016/j.earscirev.2017.04.004

Evenstar, L. A., Stuart, F. M., Hartley, A. J., & Tattich, B. (2015). Slow Cenozoic uplift of the western Andean Cordillera indicated by cosmogenic 3He in alluvial boulders from the Pacific Planation Surface. *Geophysical Research Letters*, *42*, 8448–8455. https://doi.org/10.1002/2015gl065959

Faccenna, C., Oncken, O., Holt, A. F., & Becker, T. W. (2017). Initiation of the Andean orogeny by lower mantle subduction. *Earth and Planetary Science Letters*, *463*, 189–201. https://doi.org/10.1016/j.epsl.2017.01.041

Fagereng, A., & Sibson, R. H. (2010). Melange rheology and seismic style. *Geology*, *38*(8), 751–754. https://doi.org/10.1130/G30868.1

Friederich, W., Lambrecht, L., Stöckhert, B., Wassmann, S., & Moos, C. (2014). Seismic visibility of a deep subduction channel—Insights from numerical simulation of high-frequency seismic waves emitted from intermediate depth earthquakes. *Solid Earth*, *5*(1), 141–159. https://doi.org/10.5194/se-5-141-2014

García, M., Riquelme, R., Farías, M., Hérail, G., & Charrier, R. (2011). Late Miocene-Holocene canyon incision in the western Altiplano, northern Chile: Tectonic or climatic forcing? *Journal of the Geological Society (London)*, *168*(4), 1047–1060. https://doi.org/10.1144/0016-76492010-134

Geersen, J., Ranero, C. R., Barckhausen, U., & Reichert, C. (2015). Subducting seamounts control interplate coupling and seismic rupture in the 2014 Iquique earthquake área. *Nature Communications*, *6*(1), 8267. https://doi.org/10.1038/ncomms9267

Gerbault, M., Cembrano, J., Mpodozis, C., Farias, M., & Pardo, M. (2009). Continental margin deformation along the Andean subduction zone: Thermo-mechanical models. *Physics of the Earth and Planetary Interiors*, *177*(3-4), 180–205. https://doi.org/10.1016/j.pepi.2009.09.001

Gerya, T. V., & Stöckhert, B. (2002). Exhumation rates of high pressure metamorphic rocks in subduction channels: The effect of rheology. *Geophysical Research Letters*, *29*(8), 1261. https://doi.org/10.1029/2001GL014307

Gerya, T. V., Stöckhert, B., & Perchuk, A. L. (2002). Exhumation of high-pressure metamorphic rocks in a subduction channel: A numerical simulation. *Tectonics*, *21*(6), 1056. https://doi.org/10.1029/2002tc001406

González, G., Cembrano, J., Carrizo, D., Macci, A., & Schneider, H. (2003). The link between forearc tectonics and Pliocene-Quaternary deformation of the Coastal Cordillera, northern Chile. *Journal of South American Earth Sciences*, *16*(5), 321–342. https://doi.org/10.1016/s0895-9811(03)00100-7

Hartley, A. J., & Rice, C. M. (2005). Controls on supergene enrichment of porphyry copper deposits in the Central Andes: A review and discussion. *Mineralium Deposita*, *40*(5), 515–525. https://doi.org/10.1007/s00126-005-0017-7

Hergarten, S., Robl, J., & Stüwe, K. (2014). Extracting topographic swath profiles across curved geomorphic features. *Earth Surface Dynamics*, *2*(1), 97–104. https://doi.org/10.5194/esurf-2-97-2014

Isacks, B. L. (1988). Uplift of the central Andean plateau and bending of the Bolivian orocline. *Journal of Geophysical Research*, *93*(B4), 3211–3231. https://doi.org/10.1029/JB093iB04p03211

Janiszewski, H. A., & Abers, G. A. (2015). Imaging the plate interface in the Cascadia seismogenic zone: New constraints from offshore receiver functions. *Seismological Research Letters*, *86*(5), 1261–1269. https://doi.org/10.1785/0220150104

Jordan, T. E., Kirk-Lawlor, N. E., Blanco, N., Rech, J. A., & Cosentino, N. J. (2014). Landscape modification in response to repeated onset of hyperarid paleoclimate states since 14 Ma, Atacama Desert, Chile. *Geological Society of America Bulletin*, *126*(7-8), 1016–1046. https://doi.org/10.1130/b30978.1

Jordan, T. E., Nester, P. L., Blanco, N., Hoke, G. D., Dávila, F., & Tomlinson, A. J. (2010). Uplift of the Altiplano-Puna plateau: A view from the west. *Tectonics*, *29*, TC5007. https://doi.org/10.1029/2010tc002661

Juez-Larré, J., Kukowski, N., Dunai, T. J., Hartley, A. J., & Andriessen, P. A. M. (2010). Thermal and exhumation history of the Coastal Cordillera arc of northern Chile revealed by thermochronological dating. *Tectonophysics*, *495*(1-2), 48–66. https://doi.org/10.1016/j.tecto.2010.06.018

Karig, D. E., & Kay, R. W. (1981). Fate of sediments on the descending plate at convergent margins. *Philosophical Transactions of the Royal Society A*, *301*(1461), 233–251. https://doi.org/10.1098/rsta.1981.0108

Lallemand, S. E., Schnürle, P., & Malavieille, J. (1994). Coulomb theory applied to accretionary and nonaccretionary wedges: Possible causes for tectonic erosion and/or frontal accretion. *Journal of Geophysical Research*, *99*(B6), 12,033–12,055. https://doi.org/10.1029/94jb00124

Lamb, S., & Davis, P. (2003). Cenozoic climate change as a possible cause for the rise of the Andes. *Nature*, *425*(6960), 792–797. https://doi.org/10.1038/nature02049

Madella, A., Delunel, R., Audin, L., & Schlunegger, F. (2016). Why is there no Coastal Cordillera at the Arica Bend (Western Central Andes)? *Basin Research*, *30*, 248–268. https://doi.org/10.1111/bre.12218

Melnick, D. (2016). Rise of the central Andean coast by earthquakes straddling the Moho. *Nature Geoscience*, *9*(5), 401–407. https://doi.org/10.1038/ngeo2683

Mortimer, C., & Sarič, N. (1975). Cenozoic studies in northernmost Chile. *Geologische Rundschau*, *64*(1), 395–420. https://doi.org/10.1007/bf01820676

Nester, P. (2008). Basin and paleoclimate evolution of the Pampa del Tamarugal forearc valley, Atacama Desert, northern Chile [Ph.D. thesis]: Cornell University, 273 p.

Plank, T., & Langmuir, C. H. (1998). The chemical composition of subducting sediment and its consequences for the crust and mantle. *Chemical Geology*, *145*(3-4), 325–394. https://doi.org/10.1016/S0009-2541(97)00150-2

Ranero, C. R., Grevemeyer, I., Sahling, U., Barckhausen, U., Hensen, C., Wallmann, K., et al. (2008). The hydrogeological system of erosional convergent margins and its influence on tectonics and interplate seismogenesis. *Geochemistry, Geophysics, Geosystems*, *9*, Q03S04. https://doi.org/10.1029/2007gc001679

Ranero, C. R., & von Huene, R. (2000). Subduction erosion along the Middle America convergent margin. *Nature*, *404*(6779), 748–752. https://doi.org/10.1038/35008046

Roy, M., & Royden, L. G. (2000). Crustal rheology and faulting at strike-slip plate boundaries. 1. An analytic model. *Journal of Geophysical Research*, *105*(B3), 5583–5597. https://doi.org/10.1029/1999JB900339

Sage, F., Collot, J.-Y., & Ranero, R. (2006). Interplate patchiness and subduction-erosion mechanisms: Evidence from depth-migrated seismic images at the Central Ecuador convergent margin. *Geology*, *34*(12), 997–1000. https://doi.org/10.1130/g22790a.1

Schlunegger, F., Kober, F., Zeilinger, G., & von Rotz, R. (2010). Sedimentology-based reconstructions of paleoclimate changes in the Central Andes in response to the uplift of the Andes, Arica region between 19 and 21°S latitude, northern Chile. *International Journal of Earth Sciences*, *99*(S1), 123–137. https://doi.org/10.1007/s00531-010-0572-8

Schweller, W. J., Kulm, L. D., & Prince, R. A. (1981). Tectonics, structure, and sedimentary framework of the Peru-Chile trench. *Geological Society of America Memoirs*, *154*, 323–349. https://doi.org/10.1130/MEM154-p323

Shewchuk, J. R. (1996), Triangle: Engineering a 2D quality mesh generator and Delaunay triangulator. In Applied Computational Geometry: Towards Geometric Engineering (Ming C. Lin and Dinesh Manocha, editors), *Lecture Notes in Computer Science 1148*, 203–222, Springer-Verlag, Berlin (from the First ACM Workshop on Applied Computational Geometry). https://doi.org/10.1007/BFb0014497

Shreve, R. L., & Cloos, M. (1986). Dynamics of sediment subduction, melange formation, and prism accretion. *Journal of Geophysical Research*, *91*(B10), 10,229–10,245. https://doi.org/10.1029/JB091iB10p10229

Sillitoe, R. H., & McKee, E. H. (1996). Age of supergene oxidation and enrichment in the chilean porphyry copper province. *Economic Geology*, *91*(1), 164–179. https://doi.org/10.2113/gsecongeo.91.1.164

Sobolev, S. V., & Babeyko, A. Y. (2005). What drives orogeny in the Andes? *Geology*, *33*(8), 617–620. https://doi.org/10.1130/g21557ar.1

Somoza, R. (1998). Updated Nazca (Farallon)-South America relative motions during the last 40 My: Implications for mountain building in the central Andean region. *Journal of South American Earth Sciences*, *11*(3), 211–215. https://doi.org/10.1016/S0895-9811(98)00012-1

Stöckhert, B. (2002). Stress and deformation in subduction zones: Insight from the record of exhumed metamorphic rocks. *Geological Society, London, Special Publications*, *200*(1), 255–274. https://doi.org/10.1144/gsl.sp.2001.200.01.15

Tassara, A., Götze, H.-J., Schmidt, S., & Hackney, R. (2006). Three-dimensional density model of the Nazca plate and the Andean continental margin. *Journal of Geophysical Research*, *111*, B09404. https://doi.org/10.1029/2005jb003976

van Dinther, Y., Gerya, T. V., Dalguer, L. A., Mai, P. M., Morra, G., & Giardini, D. (2013). The seismic cycle at subduction thrusts: Insights from seismo-thermo-mechanical models. *Journal of Geophysical Research: Solid Earth*, *118*, 6183–6202. https://doi.org/10.1002/2013jb010380

Vannucchi, P., Remitti, F., & Bettelli, G. (2008). Geological record of fluid flow and seismogenesis along an erosive subducting plate boundary. *Nature*, *451*(7179), 699–703. https://doi.org/10.1038/nature06486

Vannucchi, P., Sage, F., Morgan, J. P., Remitti, F., & Collot, J.-Y. (2012). Toward a dynamic concept of the subduction channel at erosive convergent margins with implications for interplate material transfer. *Geochemistry, Geophysics, Geosystems*, *13*, Q02003. https://doi.org/10.1029/2011gc003846

von Huene, R., & Lallemand, S. (1990). Tectonic erosion along the Japan and Peru convergent margins. *Geological Society of America Bulletin*, *102*(6), 704–720. https://doi.org/10.1130/0016-7606(1990)102<0704:TEATJA>2.3.CO;2

von Huene, R., & Ranero, C. R. (2003). Subduction erosion and basal friction along the sediment-starved convergent margin of Antofagasta, Chile. *Journal of Geophysical Research*, *108*(B2), 2079. https://doi.org/10.1029/2001jb001569

von Huene, R., Ranero, C. R., & Vannucchi, P. (2004). Generic model of subduction erosion. *Geology*, *32*(10), 913–916. https://doi.org/10.1130/g20563.1

Ward, K. M., Porter, R. C., Zandt, G., Beck, S. L., Wagner, L. S., Minaya, E., & et al. (2013). Ambient noise tomography across the Central Andes. *Geophysical Journal International*, *194*(3), 1559–1573. https://doi.org/10.1093/gji/ggt166

Zachos, J., Pagani, N., Sloan, L., Thomas, E., & Billups, K. (2001). Trends, rhythms, and aberrations in the global climate 65 Ma to present. *Science*, *292*(5517), 686–693. https://doi.org/10.1126/science.1059412

Zindler, A., & Hart, S. (1986). Chemical geodynamics. *Annual Review of Earth and Planetary Sciences*, *14*(1), 493–571. https://doi.org/10.1146/annurev.ea.14.050186.002425